Building compact dislocation cores in an elasto-plastic model of dislocation fields

K. Gbemou, V. Taupin, J.M. M Raulot, Claude Fressengeas

Building compact dislocation cores in an elasto-plastic model of dislocation fields

K. Gbemou, *V. Taupin, J.M. Raulot, C. Fressengeas

[1] *Laboratoire d'Etude des Microstructures et de Mécanique des Matériaux, Université de Lorraine/CNRS, Ile du Saulcy, 57045 Metz Cedex, France*

Abstract

An elasto-plastic theory of dislocation fields, where dislocation motion is accounted for by a dissipative dislocation density transport framework, is used to model in a continuous way planar dislocation core structures at nanoscale. A one-dimensional model for mixed edge/screw dislocations is developed. In order to avert endless relaxation of arbitrary initial dislocation core profiles and obtain convergence toward a compact equilibrium core structure, a Peierls-Nabarro-type misfit surface energy is introduced in the free energy density, leading to a restoring term in the driving force for dislocation motion. When using the Peierls sinusoidal potential for the restoring stress, arbitrary initial dislocation core profiles converge by relaxation towards the Peierls-Nabarro analytical solution, which corresponds to a minimum energy configuration. The model is extended by using generalized planar stacking

*Corresponding author: vincent.taupin@univ-lorraine.fr

fault energies. Basal and prismatic planar energies are obtained in titanium and zirconium from ab-initio and molecular statics simulations. Dissociation of basal edge and screw dislocations into partial mixed dislocations is predicted, whereas dissociated dislocations with partial Burgers vectors colinear to the Burgers vectors of the full dislocations are found in prismatic planes. Motion, deformation and anelastic relaxation mechanisms of dislocation cores under applied stresses are predicted by the model, as well as dislocation loop nucleation. In particular, deformation of the dislocation core under high stresses reduces the velocity of the dislocation and produces kinematic hardening at the core level.

---

1. Introduction

The celebrated Peierls-Nabarro model (Peierls,1940; Nabarro,1947) raised the fundamental question of the equilibrium configuration of a dislocation core in a crystal lattice from a continuum mechanics standpoint. Originally developed for planar dislocation cores, the Peierls-Nabarro model represents the core of a dislocation as a continuous dislocation density distribution, whose integration over the core area yields the Burgers vector. An equilibrium spatial distribution of the dislocation densities and the associated elastic displacement discontinuity, the so-called misfit, are found when the internal shear stress due to the dislocation core is counter-balanced by a lattice restoring stress. The latter originates from a non-convex periodic lattice misfit energy reflecting the resistance of the crystal to shear. Motivated by

the success of this model, recent refined models have proposed to replace the Peierls sinusoidal misfit potential by generalized stacking fault energies obtained from atomistic calculations, which renders the model more realistic (Joós,1994; Hartford,1998; Lu,2000; Schoeck,2012; Wang,2014). Instead of using a one-dimensional potential, these models rather introduce a two-dimensional energy that provides the shear resistance in all directions of a given glide plane. A striking feature of such models is their capability to predict the dissociation of dislocations into partials. Recent phase field-type models were also shown to be able to capture the evolution of dislocation cores in different slip planes in three dimensional settings (Denoual,2004; Shen,2004; Hunter,2014), the non-planar structure of dislocation cores in BCC metals (Denoual,2007) and dislocation kinks (Wei,2009). The effects of solutes on dislocation motion, dislocation / grain boundary interactions, dislocation cross slip and twinning were also investigated by using such Peierls-Nabarro based frameworks (Hu,2004; Zeng,2016; Lu,2004; Pi,2016).

In the present paper, we propose to model planar dislocation cores within a recent elasto-plastic theory of dislocation fields (Acharya,2001). In this theory, the net Burgers vector of dislocation ensembles is captured through Nye's polar dislocation density tensor (Nye,1953). The latter is a continuous rendition, with divergence-free character, of the discontinuity of the elastic/plastic displacement induced by the dislocation ensemble. When this ensemble reduces to a single dislocation, the dislocation density field smoothly describes

the dislocation core in the manner of the Peierls-Nabarro model, which allows regularizing its singular description. The elasto-static part of the theory naturally retrieves the elastic fields of a single dislocation, which it regularizes in the core region (Roy,2005). Beyond this static description, the theory also provides for the spatiotemporal evolution of a dislocation density field within a rigorous dissipative transport framework (Acharya,2003). Dislocation motion is ruled by the dislocation transport equation (Mura,1963), which expresses the conservation of the flux of the divergence-free dislocation density tensor, *i.e.* the Burgers vector, across elementary surfaces. When the dislocation ensemble reduces to a single dislocation, the dislocation velocity field describes the (possibly heterogeneous) motion of the differential dislocation elements. Hence, Peach-Koehler-type forces drive the motion of dislocation densities for the production of plastic deformation, including by possible deformation of the core. The elasto-plastic theory of dislocation fields is thus well adapted for the elasto-plastic investigation of the structure and dynamics of dislocation cores. It was also recently shown, by using a crossover method that derives kinematic fields from atomic structures (Tucker,2015), that such a framework can be applied to grain boundary core structures (Sun,2016).

The objective of the present paper is to evidence the ability of the mechanical theory of dislocation fields to predict realistic compact dislocation cores and their dynamics under loading. More precisely, the predictive capabilities brought about by the introduction of a non convex peri-

odic misfit surface energy in the free energy density are discussed, and it is shown how restoring stresses arising from this surface energy may yield compact equilibrium core structures, by self-relaxation of arbitrary initial core configurations. In Section 2, the elasto-plastic theory of dislocation fields (Acharya,2001; Acharya,2003) is briefly recalled. A one-dimensional model is derived in Section 3 for mixed edge/screw dislocation cores. It is shown that, in the absence of a restoring force, endless relaxation of dislocation cores occurs. In Section 4, we show how to introduce a Peierls-type misfit energy in the formulation and how to derive from the latter the restoring force counter-balancing the above relaxation. Note that such a procedure was independently and recently proposed by Zhang et al (Zhang,2015). The present formulation is validated by comparison with the Peierls-Nabarro analytical solution for a sinusoidal restoring force. Following recent papers (e.g. (Shen,2004; Wei,2009)), the model is further developed in Section 5, in order to use generalized planar stacking fault energies as an input for the misfit energy and to describe dissociation of dislocations into partials. This extended model is applied to edge and screw dislocations in basal and prismatic planes in titanium and zirconium, by using stacking fault energies as obtained from atomistic calculations. In Section 6, the model is finally used to investigate the motion and deformation of dislocation cores under applied stresses, and the nucleation of dislocation loops under localized shear stress. Conclusions follow. In the Appendix, we provide details about the numerical calculations of generalized stacking faults energies in Zr and Ti, as well as useful

mathematical notations.

2. Elasto-plastic model of dislocation fields

2.1. Incompatibility

In a small strain setting, the total distortion $\mathbf{U}$ of a continuum body elasto-plastically deformed is decomposed into elastic $\mathbf{U}^e$ and plastic $\mathbf{U}^p$ parts, such that $\mathbf{U} = \mathbf{U}^e + \mathbf{U}^p$. Because the total material displacement vector field $\mathbf{u}$ is continuously differentiable, the total distortion tensor can be defined as the gradient of that vector field. As such, it is curl-free. The following relations then hold:

$$\mathbf{U} = \mathbf{grad}\,\mathbf{u}, \tag{1}$$

$$\mathbf{curl}\,\mathbf{U} = \mathbf{0}. \tag{2}$$

In the presence of a dislocation or a polarised ensemble of dislocations, the occurrence of a non-zero net Burgers vector $\mathbf{b}$ induces a discontinuity of the elastic and plastic displacement vector fields. Hence, in addition to compatible curl-free parts $\mathbf{U}^{e\|}$ and $\mathbf{U}^{p\|}$, the elastic and plastic distortion tensors additionally contain incompatible parts $\mathbf{U}^{e\perp}$ and $\mathbf{U}^{p\perp}$ that are not gradients. Their non-zero curl defines Nye's polar dislocation density tensor $\boldsymbol{\alpha}$ (Nye,1953), such that (Kröner,1980)

$$\boldsymbol{\alpha} = \mathbf{curl}\,\mathbf{U}^{e\perp} = -\mathbf{curl}\,\mathbf{U}^{p\perp}. \tag{3}$$

Being a curl, it is clear that $\boldsymbol{\alpha}$ is a divergence-free tensor. Because the curl operator extracts the incompatible part of a tensor, Eq.(3) implies

$$\boldsymbol{\alpha} = \mathbf{curl}\, \mathbf{U}^e = -\mathbf{curl}\, \mathbf{U}^p. \tag{4}$$

The total distortion reads $\mathbf{U} = \mathbf{U}^e + \mathbf{U}^p = \mathbf{U}^{e\|} + \mathbf{U}^{p\|} + \mathbf{U}^{e\perp} + \mathbf{U}^{p\perp}$. To ensure that it is a curl-free tensor, the sum of incompatible parts $\mathbf{U}^{e\perp} + \mathbf{U}^{p\perp} = \mathbf{0}$ and $\mathbf{U} = \mathbf{U}^{e\|} + \mathbf{U}^{p\|}$. Given a surface S of unit normal $\mathbf{n}$ bounded by a closed circuit C, Eq.(4) derives from

$$\mathbf{b} = \oint_C \mathbf{U}^e\, dx = \int_S \mathbf{curl}\, \mathbf{U}^e.\mathbf{n}\, dS = \int_S \boldsymbol{\alpha}.\mathbf{n}\, dS. \tag{5}$$

In a cartesian frame $(\mathbf{e}_1, \mathbf{e}_2, \mathbf{e}_3)$, the components of the tensor $\boldsymbol{\alpha}$ write $\alpha_{ij} = b_i t_j$, where b_i is an areal density of Burgers vector along direction $\mathbf{e}_i$ (in units of $m/m^2 = m^{-1}$) and t_j is the component of the dislocation line vector along direction $\mathbf{e}_j$.

2.2. Elasticity

Eq.(4) clearly shows that the presence of a polar dislocation density within a continuum body induces long-range internal elastic distortions. A free energy density $\psi = \psi(\boldsymbol{\epsilon}^e)$ is assumed, where $\boldsymbol{\epsilon}^e$ denotes the elastic strain tensor. The stress tensor $\mathbf{T} = \partial\psi/\partial\boldsymbol{\epsilon}^e$ has to satisfy the balance of momentum $\mathbf{divT} = \mathbf{0}$ in the absence of body forces and under quasi-static conditions. By assuming homogeneous linear isotropic elasticity with a fourth-order elastic moduli

tensor $\mathbf{C}$, the balance equation reads

$$\mathbf{divT} = \mathbf{div}(\mathbf{C} : \boldsymbol{\epsilon}^e) = \mathbf{div}(\mathbf{C} : (\boldsymbol{\epsilon} - \boldsymbol{\epsilon}^p)) = \mathbf{0}, \tag{6}$$

where the total strain tensor $\boldsymbol{\epsilon} = (\mathbf{gradu})^{sym}$ is the unknown and $\boldsymbol{\epsilon}^p$ derives from the distribution and evolution of polar dislocation densities. The mathematical procedure and numerical approximations used to derive the internal stress field arising from a given spatial distribution of dislocation density $\boldsymbol{\alpha}$ can be found in refs. (Acharya,2001; Berbenni,2014). As already mentioned, a remarkable feature of the model is the non-singularity of the elastic strain and stress fields in the dislocation core region (Roy,2005).

2.3. Plasticity

Plastic straining derives from dislocation glide. In the elasto-plastic theory of dislocation fields (Acharya,2001; Acharya,2003), the incompatibility generated by dislocation motion controls the evolution of the divergence-free dislocation density tensor through the dislocation transport equation (Mura,1963):

$$\dot{\boldsymbol{\alpha}} = \frac{\partial \boldsymbol{\alpha}}{\partial t} = -\mathbf{curl}\,(\boldsymbol{\alpha} \times \mathbf{V}^{\alpha}). \tag{7}$$

In this equation, t denotes time, $\mathbf{V}^{\alpha}$ is the dislocation density velocity vector field and $\boldsymbol{\alpha} \times \mathbf{V}^{\alpha}$ is the plastic distortion rate arising from the motion of the polar dislocation densities $\boldsymbol{\alpha}$. Eq.(7) provides the evolution of the divergence-free dislocation density tensor $\boldsymbol{\alpha}$ that is compatible with the con-

servation of its flux through arbitrary patches, *i.e.* the Burgers vector of the dislocations threading these patches. Of course, this property holds irrespective of the magnitude and orientation of the latter, which may well be relative to a differential dislocation element. By introducing an independent incompatible plastic distortion rate $\dot{\mathbf{U}}^{p*} = \mathbf{curl}\,\mathbf{S}$ associated with the nucleation/cancellation of dislocation densities, the total plastic distortion rate $\dot{\mathbf{U}}^{p}$ becomes

$$\dot{\mathbf{U}}^{p} = \boldsymbol{\alpha} \times \mathbf{V}^{\alpha} + \dot{\mathbf{U}}^{p*} = \boldsymbol{\alpha} \times \mathbf{V}^{\alpha} + \mathbf{curl}\,\mathbf{S}. \tag{8}$$

In this case, the dislocation density tensor ceases to be divergence-free, and Eq.(7) includes a source/sink term:

$$\dot{\boldsymbol{\alpha}} = \frac{\partial \boldsymbol{\alpha}}{\partial t} = -\mathbf{curl}\,(\boldsymbol{\alpha} \times \mathbf{V}^{\alpha}) - \mathbf{curl}\,(\mathbf{curl}\,\mathbf{S}). \tag{9}$$

In the present context, the meaning of the dislocation source/sink term $-\mathbf{curl}\,(\mathbf{curl}\,\mathbf{S})$ is as follows: if the plastic distortion rate $\boldsymbol{\alpha} \times \mathbf{V}^{\alpha}$ of the existing polar dislocation densities is too constrained to allow thorough relaxation of the elastic energy, then $\dot{\mathbf{U}}^{p*}$ may generate independent plastic distortions potentially able to complete relaxation by allowing the nucleation of additional dislocations. Of course, this term should be energetically harder to activate than the dislocation mobility. Note that the Stokes-Helmholtz decomposition of $\dot{\mathbf{U}}^{p*}$ generally contains a compatible gradient part, $\mathbf{grad}\,\mathbf{N}$, in addition to the incompatible curl part, $\mathbf{curl}\,\mathbf{S}$, such that $\dot{\mathbf{U}}^{p*} = \mathbf{grad}\,\mathbf{N} + \mathbf{curl}\,\mathbf{S}$. Taking the curl of $\dot{\mathbf{U}}^{p*}$ leaves out the compati-

ble part, so that only the incompatible part **curl** (**curl S**) is retained in the transport equation (9). This is because we want to ensure that, in absence of dislocation mobility, plasticity is produced only through the corresponding nucleation of a dislocation density in the crystal. Plasticity may alternatively derive from grain boundary mechanisms, such as grain boundary migration or grain rotation/dislocation emission, but these processes involve the incompatibility of curvature and are beyond the scope of the present manuscript (Taupin,2014). The field $\mathbf{S}$ can thus be seen as a nucleation potential. Constitutive relationships for the velocity of dislocation densities $\mathbf{V}^{\alpha}$ and for $\dot{\mathbf{U}}^{p*}$ will be derived from thermodynamical considerations (Acharya,2003) in the next subsection.

2.4. Mechanical dissipation

The mechanical dissipation D in a continuum body V is defined as the difference between the power of the applied forces and the rate of change of the stored energy:

$$D = \int_{\partial V} \mathbf{v}.\mathbf{T}.\mathbf{n} dS - \int_V \dot{\psi} dv = \int_{\partial V} v_i T_{ij} n_j dS - \int_V \dot{\psi} dv. \qquad (10)$$

In Eq.(10), $\mathbf{v}$ is the material velocity vector field and $\mathbf{T}.\mathbf{n}$ is the stress vector applied on the external boundary ∂V of unit normal $\mathbf{n}$. Volumetric forces are ignored for the sake of simplicity. The power dissipation D can be rewritten

as (Acharya,2003; Fressengeas,2011)

$$D = \int_V (\mathbf{T} : \dot{\boldsymbol{\epsilon}} - \dot{\psi}) dv. \tag{11}$$

Assuming that $\psi = \psi(\boldsymbol{\epsilon}^e)$, the rate of change of the stored energy is $\dot{\psi} = (\partial\psi/\partial\boldsymbol{\epsilon}^e) : \dot{\boldsymbol{\epsilon}}^e = \mathbf{T} : \dot{\boldsymbol{\epsilon}}^e$ and the dissipation becomes

$$D = \int_V \mathbf{T} : \dot{\boldsymbol{\epsilon}}_p \, dv. \tag{12}$$

We now substitute the plastic strain rate $\dot{\boldsymbol{\epsilon}}_p = (\dot{\mathbf{U}}^p)^{sym}$ for its expression in Eq.(12). In component form, we obtain:

$$D = \int_V (e_{jkl} T_{ij} \alpha_{ik} V_l^\alpha + T_{ij} \dot{\epsilon}_{ij}^{p*}) dv = \int_V (\mathbf{F}^\alpha . \mathbf{V}^\alpha + \mathbf{T} : \dot{\boldsymbol{\epsilon}}^{p*}) dv. \tag{13}$$

The vector $\mathbf{F}^\alpha$, in component form $F_l^\alpha = e_{jkl} T_{ij} \alpha_{ik}$, is a Peach-Koehler type driving force for the motion of the polar dislocation density $\boldsymbol{\alpha}$. $\dot{\boldsymbol{\epsilon}}^{p*}$ is the symmetric part of $\dot{\mathbf{U}}^{p*}$. From the second law of thermodynamics, the mechanical dissipation D must be positive. To this end, we assume the simple following independent constitutive relations for $\mathbf{V}^\alpha$ and $\dot{\boldsymbol{\epsilon}}^{p*}$:

$$\mathbf{V}^\alpha = \frac{\mathbf{F}^\alpha}{B^\alpha}; \quad B^\alpha > 0 \tag{14}$$

$$\dot{\boldsymbol{\epsilon}}^{p*} = \dot{\gamma}^{p*} \frac{\mathbf{T}}{T^*}; \quad \dot{\gamma}^{p*} > 0, T^* > 0 \tag{15}$$

where B_α, T^* and $\dot{\gamma}^{p*}$ are positive material parameters. B_α is a drag coefficient, T^* and $\dot{\gamma}^{p*}$ are reference stress and plastic strain rate constants, respectively. Not done in the present paper where only shear deformation is considered, the deviatoric part of the stress tensor may easily be substituted for the Cauchy stress tensor in Eq.(15) and a modified expression of the dislocation driving force (Fressengeas,2011b) may be used in order to impose plastic incompressibility.

3. One-dimensional model for planar dislocation cores

3.1. Field equations

In the reference cartesian frame $(\mathbf{e}_1, \mathbf{e}_2, \mathbf{e}_3)$, we define a single glide plane $(\mathbf{e}_1, \mathbf{e}_3)$ of unit normal $\mathbf{e}_2$. We consider infinitely straight dislocation lines aligned with the $\mathbf{e}_3$ axis. Dislocation lines can have both edge and screw Burgers vector components. For a pure edge dislocation, the Burgers vector is along the axis $\mathbf{e}_1$, while for a pure screw dislocation it is along the axis $\mathbf{e}_3$. Dislocation lines are then assume to glide straightly along the direction $\mathbf{e}_1$. To model such a situation, we thus assume a distribution of infinitely straight differential dislocation elements along the $\mathbf{e}_3$ direction. The model is invariant along this direction, *i.e.* $\partial/\partial x_3 = 0$. The edge and screw dislocation elements correspond to the polar dislocation densities α_{13} and α_{33}, respectively. In the case of planar dislocation cores, the elasto-plastic model of dislocation fields reduces to a one-dimensional formulation for the spatiotemporal evolution of the polar dislocation densities $\alpha_{13}(x_1)$ and $\alpha_{33}(x_1)$. If d denotes the

interplanar distance between two consecutive glide planes, the surface dislocation densities α_{13}^S and α_{33}^S (adimensional line density) are related to the polar dislocation densities (dimensional surface density) through the relations $\alpha_{13} = \alpha_{13}^S/d$ and $\alpha_{33} = \alpha_{33}^S/d$. This surface representation can be viewed as a one-dimensional simplification of the recent dislocation layer model of Zhang et al (Zhang,2015), where the dislocation core and its slip plane are supported by a layer of small but non-zero thickness. Given a distribution of surface dislocations $\alpha_{13}^S(x_1)$ and $\alpha_{33}^S(x_1)$ and assuming homogeneous linear isotropic elasticity, the associated internal shear stress fields in the glide plane are obtained from the following convolution integrals (Peierls,1940; Nabarro,1947):

$$T_{12}(x_1) = \frac{\mu}{2\pi(1-\nu)} \int_{-\infty}^{+\infty} \frac{\alpha_{13}^S(x_1')}{(x_1 - x_1')} dx_1', \tag{16}$$

$$T_{32}(x_1) = \frac{\mu}{2\pi} \int_{-\infty}^{+\infty} \frac{\alpha_{33}^S(x_1')}{(x_1 - x_1')} dx_1', \tag{17}$$

where μ and ν denote the shear modulus and Poisson coefficient, respectively. In the forthcoming simulations, using such infinite medium expressions requires external boundaries to be set out sufficiently far from the dislocation core. According to Eqs.(8,14,15), the plastic strain rates $\dot{\epsilon}_{12}^p$ and $\dot{\epsilon}_{32}^p$ are:

$$\dot{\epsilon}_{12}^p = \frac{1}{2}\alpha_{13}\, V_1^{\alpha_{13}} + \dot{\gamma}^{p*}\frac{T_{12}}{T^*} = \frac{1}{2}\alpha_{13}\, \frac{T_{12}\alpha_{13}}{B^\alpha} + \dot{\gamma}^{p*}\frac{T_{12}}{T^*}, \tag{18}$$

$$\dot{\epsilon}_{32}^p = \frac{1}{2}\alpha_{33}\, V_1^{\alpha_{33}} + \dot{\gamma}^{p*}\frac{T_{32}}{T^*} = \frac{1}{2}\alpha_{33}\, \frac{T_{32}\alpha_{33}}{B^\alpha} + \dot{\gamma}^{p*}\frac{T_{32}}{T^*}. \tag{19}$$

The transport equation (9) reduces to:

$$\dot{\alpha}_{13} = -(\alpha_{13}\, V_1^{\alpha_{13}} + \dot{\gamma}^{p*}\frac{T_{12}}{T^*})_{,1}\ , \tag{20}$$

$$\dot{\alpha}_{33} = -(\alpha_{33}\, V_1^{\alpha_{33}} + \dot{\gamma}^{p*}\frac{T_{32}}{T^*})_{,1}\ , \tag{21}$$

where $f_{,1}$ denotes the partial derivative of f with respect to x_1. Eqs.(16,18,20) are used to model the relaxation of an initially compact edge dislocation core in the next subsection. Material parameters for Al are used: $\mu = 28GPa$, $\nu = 0.3$. The magnitude of Burgers vector is $b = 0.405nm$, and $d = 0.36nm$. For the drag coefficient, we use the value $B^\alpha = B_r/b^2 = 10^{15}Pa.s.m^{-2}$, where $B_r \approx 10^{-4}Pa.s$ is a typical value at room temperature in Al. As aforementioned, the value of B^α being fixed, a sufficiently small value of $\dot{\gamma}^{p*} = 10^{-10}s^{-1}$ and a sufficiently large value $T^* = 5GPa$ are arbitrarily chosen to ensure that dislocation mobility prevails over dislocation nucleation.

3.2. Endless self-relaxation of an edge dislocation core

The length L_1 of the glide plane along glide direction $\mathbf{e}_1$ is $25nm$. The sample is discretised into 1000 elements (1001 nodes), which implies a spatial resolution of $0.025nm$, sufficient to reach an accurate description of the dislocation cores. In a general three-dimensional setting, the numerical approximation of the dislocation transport equation can be done either by using a mixed Galerkin - Least squares finite element scheme (Varadhan,2006), or by using filtered spectral approaches (Djaka,2015). The common feature of these numerical approaches is the introduction of damping terms that

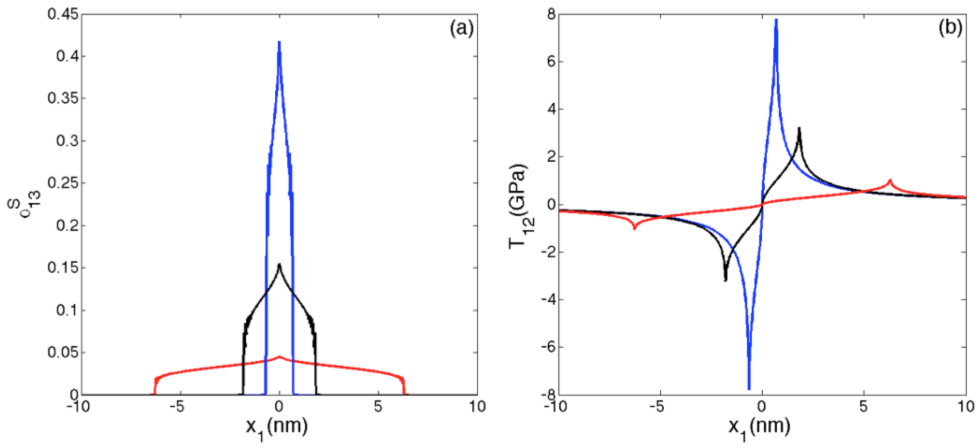

Figure 1: Endless relaxation of an edge dislocation core under its own internal stress field. Blue, black and red snapshot curves show progressive spreading of the core, until it completely disappears from the plane. (a): edge dislocation density α_{13}^S. (b): internal shear stress field T_{12}.

smooth out possible numerical instabilities that might generate and propagate due to the hyperbolic character of the transport equation. In the present one-dimensional setting however, the spatial derivatives that appear in the transport equations (20,21) can be approximated by a simple Euler upwind or Euler centered scheme and the dislocation densities can be updated by using a simple explicit time integration. Additional artificial diffusion can also be easily added (finite difference scheme) to smooth out possible numerical fluctuations and stabilize the solution (Varadhan,2006). As shown in Fig.(1), a compact edge dislocation density distribution α_{13}^S is initially introduced in the middle of the glide plane, such that the associated Burgers vector is $\int_{L_1} \alpha_{13}^S dx_1 = b$. Because the dislocation density distribution feels its own shear stress field, a non-zero driving force $T_{12}\alpha_{13}$ exists, whose effect is

to spread out the dislocation core. Two criteria are used to check whether an equilibrium structure is reached during self-relaxation, namely: (1) the relative decay of the dislocation energy between two time steps becomes smaller than a very small value, and (2) the difference of the dislocation density between two time steps (least square residual) becomes lower than a very small value. When these two criteria are met, the relaxation process is stopped and the dislocation ensemble is declared as having reached an equilibrated configuration. As shown in Fig.(1) however, spreading of the dislocation core is observed until the dislocation density field uniformly vanishes over the glide plane and the energy reaches zero. Such a result was also shown in the layer model of Zhang et al (Zhang,2015). Of course, this is by no means a new result, and the trend was predictable from the fact that the dislocation core is made of infinitesimal edge dislocations of the same sign repelling each other. This endless relaxation occurs because, in the above formulation, the model does not involve any opposing force to the spread of the dislocation distribution. The origin of this opposing force is the lattice friction, which opposes to dislocation glide (Chu,2013; Wang,2008; Zhang,2016). Introducing such a "restoring force" into the formulation is the object of the next section. Note also that running the same simulation without the term $\dot{\boldsymbol{\epsilon}}^{p*}$ yields exactly the same result, implying that $\dot{\boldsymbol{\epsilon}}^{p*}$ does not have any influence on this relaxation process. This is because the mobility of the edge dislocation density $\alpha_{13}V_1^{\alpha_{13}}$ is sufficient to fully relax the elastic energy.

4. Misfit energy and crystal restoring force

4.1. The Peierls-Nabarro model

It has already been suggested above that, in the Peierls-Nabarro model (Peierls,1940; Nabarro,1947), the Burgers vector is described by using a continuous spatial distribution of surface dislocation density α^S. If x denotes the glide direction axis, integrating $\alpha^S(x)$ up to x smoothly defines the misfit $\eta(x)$:

$$\eta(x) = \int_{-\infty}^{x} \alpha^S(x)dx, \tag{22}$$

$$\alpha^S(x) = \partial\eta(x)/\partial x, \tag{23}$$

which allows representing the discontinuity of the elastic displacement (or plastic displacement, up to a sign) in a regularized manner:

$$b = \int_{-\infty}^{+\infty} \alpha^S(x)dx. \tag{24}$$

Finding an equilibrium configuration of the dislocation core, *i.e.* a steady-state distribution of $\eta(x)$ and $\alpha^S(x)$, requires that the internal shear stress induced by the dislocation density $\alpha^S(x)$ be counterbalanced by a crystal restoring stress $T^R(x)$. The latter represents the reaction of the crystal to the shear stress induced by the dislocation and opposes the resulting glide. In order to trap the misfit $\eta(x)$ at multiple values of the Burgers vector b to respect the periodicity of the crystal, the restoring stress $T^R(x)$ must be

taken as a periodic function of the misfit $\eta(x)$, with period b. Initially, Peierls assumed a sinusoidal function of the form

$$T^R(x) = \mu/(2\pi)sin(2\pi\eta(x)/b). \tag{25}$$

Thus, the distribution $\eta(x)$ representing a steady-state configuration of the dislocation core is a solution of the pseudo-integral equation

$$K\int_{-\infty}^{+\infty}\frac{\alpha^S(x')}{(x-x')}dx' + \mu/(2\pi)sin(2\pi\eta(x)/b) = 0, \tag{26}$$

with $K = \frac{\mu}{2\pi(1-\nu)}$ for an edge dislocation and $K = \frac{\mu}{2\pi}$ for a screw dislocation. An analytical expression was found for $\eta(x)$:

$$\eta(x) = \frac{b}{2} + \frac{b}{\pi}atan(2x\beta/b), \tag{27}$$

where $\beta = (1-\nu)$ for an edge dislocation and $\beta = 1$ for a screw dislocation. The Peierls-Nabarro solution (27) will be used in subsection 4.3 as a benchmark for validating the elasto-plastic model of dislocation fields developed in the next subsection.

4.2. Introduction of the misfit energy and restoring stress in the model

The restoring stress proposed by Peierls assumes a contribution of the lattice misfit η to the free energy. This misfit energy is non convex and periodic. It takes the form

$$\gamma = \frac{\mu b}{4\pi^2}(1 - cos(2\pi\eta/b)), \tag{28}$$

such that its derivative with respect to η gives the restoring stress (25). We may introduce two such misfits in our model. The edge dislocation density α_{13}^S induces a misfit η_{12} regularizing the elastic displacement discontinuity in the $\mathbf{e}_1$ direction, across the glide plane of unit normal $\mathbf{e}_2$. Similarly, the screw dislocation density α_{33}^S induces a misfit η_{32} of the elastic displacement and the following relations hold:

$$\begin{aligned}
\eta_{12}(x_1) &= \int_{-\infty}^{x_1} \alpha_{13}^S(x_1)dx_1, & (29)\\
\alpha_{13}^S(x_1) &= \partial\eta_{12}(x_1)/\partial x_1, & (30)\\
\eta_{32}(x_1) &= \int_{-\infty}^{x_1} \alpha_{33}^S(x_1)dx_1, & (31)\\
\alpha_{33}^S(x_1) &= \partial\eta_{32}(x_1)/\partial x_1. & (32)
\end{aligned}$$

In the following, we restrict ourselves to the pure edge dislocation case and the screw component is disregarded. However, a mixed edge/screw model with restoring stresses derived from generalized stacking fault energies will be developed further in Section 5. Accounting for the contribution of the misfit η_{12} to the free energy density yields a total energy $\Psi = \psi(\boldsymbol{\epsilon}^e) + \gamma_{12}/d$, where $\gamma_{12} = \frac{\mu b}{4\pi^2}(1 - cos(2\pi\eta_{12}/b))$. The misfit energy γ_{12} is a surface density (in units of J/m^2) localized in the glide plane. Thus, γ_{12} is normalised by the

interplanar distance d in order to yield a volume density (in units of J/m^3) consistent with the model formulation. The rate of change of the total energy density reads:

$$\dot{\Psi} = \mathbf{T} \ : \boldsymbol{\epsilon}^e + \frac{1}{d}\frac{\partial \gamma_{12}}{\partial \eta_{12}}\dot{\eta}_{12}. \tag{33}$$

By dividing η_{12} by the interplanar distance d, taking time derivative of Eq.(30) together with Eq.(20), we identify the rate of change $\dot{\eta}_{12}$ as:

$$\dot{\eta}_{12}/d = -\alpha_{13}\, V_1^{\alpha_{13}} - \dot{U}_{12}^{p*} = -\dot{U}_{12}^{p}. \tag{34}$$

We shall now cast the rate of free energy density (33) into the mechanical dissipation framework developed in Section 2.4, and re-derive the constitutive expressions for the dislocation velocities $\mathbf{V}^\alpha$ and plastic strain rates $\dot{\boldsymbol{\epsilon}}^{p*}$. The dissipation now reads

$$D = \int_V (T_{12}\dot{\epsilon}_{12}^p + T_{21}\dot{\epsilon}_{21}^p - \frac{1}{d}\frac{\partial \gamma_{12}}{\partial \eta_{12}}\dot{\eta}_{12}\,)dv. \tag{35}$$

Because $T_{12} = T_{21}$, $\dot{\epsilon}_{12}^p = \dot{\epsilon}_{21}^p = 1/2\ \dot{U}_{12}^p$, and remembering that $\dot{\eta}_{12}/d = -\dot{U}_{12}^p$, the dissipation is finally found as

$$D = \int_V (T_{12}\dot{U}_{12}^p - \frac{\partial \gamma_{12}}{\partial \eta_{12}}\frac{\dot{\eta}_{12}}{d}\,)dv = \int_V (T_{12} + \frac{\partial \gamma_{12}}{\partial \eta_{12}})\dot{U}_{12}^p\, dv. \tag{36}$$

Hence, the constitutive and dislocation transport equations: Eq.(18) and

Eq.(20) become

$$\dot{\epsilon}^p_{12} = \frac{1}{2}\alpha_{13}\,\frac{(T_{12}+\partial\gamma_{12}/\partial\eta_{12})\alpha_{13}}{B^\alpha} + \dot{\gamma}^{p*}\frac{T_{12}+\partial\gamma_{12}/\partial\eta_{12}}{T^*}, \quad (37)$$

$$\dot{\alpha}_{13} = -(\alpha_{13}\,\frac{(T_{12}+\partial\gamma_{12}/\partial\eta_{12})\alpha_{13}}{B^\alpha} + \dot{\gamma}^{p*}\frac{T_{12}+\partial\gamma_{12}/\partial\eta_{12}}{T^*})_{,1}\,. \quad (38)$$

The relationship (16) for the shear stress T_{12} remains unchanged. The two above equations clearly show that the shear stress T_{12} driving dislocation glide is now counterbalanced by a restoring stress $T^R_{12} = \partial\gamma_{12}/\partial\eta_{12}$. Starting again, as in Section 3.2, from an initially compact edge dislocation core configuration, it is now expected that core spreading will stop at a point where the total driving force $(T_{12} + \partial\gamma_{12}/\partial\eta_{12})\alpha_{13}$ becomes sufficiently small.

4.3. Relaxed equilibrium structure of an edge dislocation core

We now apply the model to the self-relaxation of the two arbitrary initial edge dislocation distributions shown in Fig.(2.a). The first initial distribution displays the quasi-singular core used in Fig.(1). The second one has a very diffuse (large) core, much larger than the Peierls-Nabarro core solution. During relaxation, spreading of the quasi-singular distribution occurs because the shear stress T_{12} is larger than the restoring stress T^R_{12}. Conversely, the diffuse distribution is compacting because the shear stress T_{12} is lower than the restoring stress T^R_{12}. After sufficient relaxation time, at a point where the shear stress and the restoring stress cancel each other, both distributions converge towards a single compact equilibrium structure, as shown in Fig.(2.a). Strikingly, the equilibrium solution matches the Peierls-Nabarro analytical

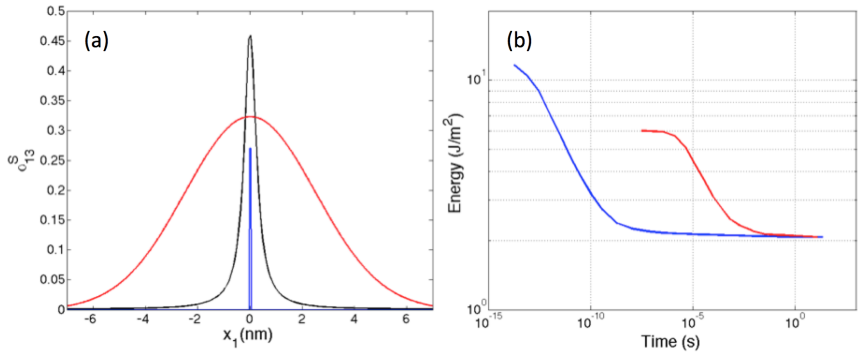

Figure 2: Initial and relaxed edge dislocation cores as obtained by using the Peierls sinusoidal potential. (a): dislocation density α^S_{13}. The blue curve is an initially compact dislocation core (amplitude divided by 30), the red curve is an initially large dislocation core (amplitude multiplied by 5) and the black curve is the dislocation core profile obtained after the self-relaxation of both compact and large dislocation cores. (b) Time-evolution of the energy associated with the self-relaxation of the compact (blue) and large (red) dislocation cores shown in (a).

solution. This is evidenced in Fig.(3), where the restoring stress is observed to exactly counterbalance the internal shear stress of the dislocation core. Note that the Peierls-Nabarro dislocation core profile is an elasto-static solution obtained from the stress balance equation (26), which does not warrant that it can be attained through a dynamical process. In contrast, the present dynamical solutions converge towards the Peierls-Nabarro solution by dissipative transport from two arbitrarily chosen initial dislocation profiles. The evolution in time of the dislocation core energies depicted in Fig.(2.b) suggests that the Peierls-Nabarro solution is actually a local minimum energy configuration. We checked again that the source term $\dot{\boldsymbol{\epsilon}}^{p*}$ does not have any influence on the above relaxation processes, because the mobility of the edge dislocation density $\alpha_{13}V_1^{\alpha_{13}}$ is sufficient to fully relax the internal energy.

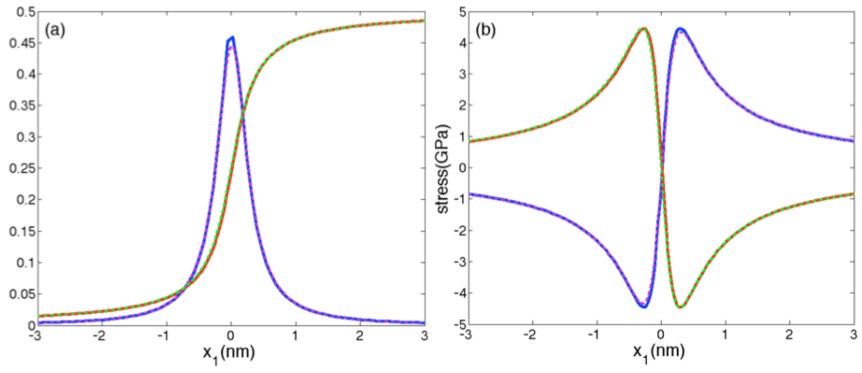

Figure 3: Relaxed configuration of an edge dislocation core as obtained by the edge model by using the Peierls sinusoidal potential. (a): the blue curve is the edge dislocation density α_{13}^S, the Peierls solution is plotted in purple dotted line. The red curve is the misfit η_{12} (in units of $2b$), the green dotted line is the Peierls solution. (b) the blue curve is the shear stress T_{12} (GPa), the Peierls solution is plotted in purple dotted line. The red curve is the restoring stress T_{12}^R (GPa), the green dotted line is the Peierls solution.

5. Introduction of generalized stacking fault energies

5.1. Stacking faults energies for Ti/Zr basal and prismatic planes

In the present one-dimensional model for planar dislocation cores, it is straightforward to substitute generalised stacking fault energies for the Peierls sinusoidal potential. Indeed, Fourier series can be defined to fit the energy landscape arising from the discrete values of a planar energy field obtained by atomistic calculations (Shen,2004; Schoeck,2012). These series provide an analytical approximation of the generalized stacking fault energy as a function of misfits, whose derivatives with respect to the misfits give access to the restoring stresses. In our case, a planar stacking fault energy function $\gamma(\eta_{12}, \eta_{32})$ is to be derived from the atomistic results. We performed such a derivation for basal and type-I prismatic planes in titanium and zirconium.

The stacking fault energies in basal planes were obtained from Ab-Initio calculations by using the Vasp software (Vasp,2015). The energies in prismatic planes were obtained by using a home-made molecular statics simulation code. Details about these calculations are provided in appendices A and B. If η_a denotes the misfit along the Burgers vector direction $< 11-20 >$ in both the basal and type-I prismatic planes, and η_b the misfit along the directions $< 1-100 >$ and $< 0001 >$ in basal and type-I prismatic planes respectively, the Fourier series takes the form:

$$\gamma(\eta_a,\eta_b) = \sum_n \sum_m A_{nm} cos(\frac{2\pi n\eta_a}{T_1}) cos(\frac{2\pi m\eta_b}{T_2}) + B_{nm} cos(\frac{2\pi n\eta_a}{T_1}) sin(\frac{2\pi m\eta_b}{T_2}) + C_{nm} sin(\frac{2\pi n\eta_a}{T_1}) cos(\frac{2\pi m\eta_b}{T_2}) + D_{nm} sin(\frac{2\pi n\eta_a}{T_1}) sin(\frac{2\pi m\eta_b}{T_2}), \quad (39)$$

where the relevant coefficients A_{nm} and B_{nm} are given in Tab.(1). The coefficients C_{nm} and D_{nm} are negligible. For the basal plane, the magnitudes of the Burgers vector along $T_1 =< 11-20 >$ and $T_2 =< 1-100 >$ directions are equal to $0.29338nm$ and $0.50816nm$ for Ti and to $0.32293nm$ and $0.55933nm$ for Zr. For the type-I prismatic plane, the magnitudes of Burgers vector along $T_1 =< 11-20 >$ and $T_2 =< 0001 >$ directions are equal to $0.29472nm$ and $0.46991nm$ for Ti and to $0.32323nm$ and $0.51717nm$ for Zr. The corresponding generalized stacking fault energy landscapes are shown in Figs.(4,5). To evidence the numerical accuracy of these calculations, we show the energy profiles along $< 1-100 >$ dissociation paths in basal planes and along $< 11-20 >$ paths in prismatic planes in the figures. For Zr, we observe a good agreement between our profiles and those provided in a

recent work (Clouet,2012). To model the relaxation of an edge dislocation α_{13} with our model, we set $\eta_a = \eta_{12}$ and $\eta_b = \eta_{32}$ in the Fourier series. For a screw dislocation α_{33}, $\eta_a = \eta_{32}$ and $\eta_b = \eta_{12}$. Note that the elastic strain energy should be removed from the generalized stacking fault energies to avoid redundancy in the total free energy density (Denoual,2007; Metsue,2010), a task not carried out in this work.

5.2. Edge/screw model for Ti/Zr basal and prismatic dislocations

The generalized stacking fault energies $\gamma(\eta_{12}, \eta_{32})$ obtained for Ti and Zr can be easily introduced in the mixed edge/screw model by substituting γ_{12}/d for $\gamma(\eta_{12}, \eta_{32})/d$ in the free energy density. The rate of change of the latter is now $\dot{\Psi} = \mathbf{T} : \dot{\boldsymbol{\epsilon}}^e + \frac{1}{d}\frac{\partial \gamma}{\partial \eta_{12}}\dot{\eta}_{12} + \frac{1}{d}\frac{\partial \gamma}{\partial \eta_{32}}\dot{\eta}_{32}$. Then, considering again the mechanical-dissipation framework derived in Section 4.2, it is easy to see that Eqs.(18,19,20,21) become:

$$\dot{\epsilon}^p_{12} = \frac{1}{2}\alpha_{13}\,\frac{(T_{12} + \partial\gamma/\partial\eta_{12})\alpha_{13}}{B^\alpha} + \dot{\gamma}^{p*}\frac{T_{12} + \partial\gamma/\partial\eta_{12}}{T^*}, \tag{40}$$

$$\dot{\epsilon}^p_{32} = \frac{1}{2}\alpha_{33}\,\frac{(T_{32} + \partial\gamma/\partial\eta_{32})\alpha_{33}}{B^\alpha} + \dot{\gamma}^{p*}\frac{T_{32} + \partial\gamma/\partial\eta_{32}}{T^*}, \tag{41}$$

$$\dot{\alpha}_{13} = -(\alpha_{13}\,\frac{(T_{12} + \partial\gamma/\partial\eta_{12})\alpha_{13}}{B^\alpha} + \dot{\gamma}^{p*}\frac{T_{12} + \partial\gamma/\partial\eta_{12}}{T^*})_{,1}\,, \tag{42}$$

$$\dot{\alpha}_{33} = -(\alpha_{33}\,\frac{(T_{32} + \partial\gamma/\partial\eta_{32})\alpha_{33}}{B^\alpha} + \dot{\gamma}^{p*}\frac{T_{32} + \partial\gamma/\partial\eta_{32}}{T^*})_{,1}\,. \tag{43}$$

As already mentioned, the restoring stresses $T^R_{12} = \partial\gamma/\partial\eta_{12}$ and $T^R_{32} = \partial\gamma/\partial\eta_{32}$ are calculated from the derivatives of the Fourier series expression

Table 1: Fourier series coefficients (mJ/m^2) obtained for generalised stacking fault energies in basal (b) and prismatic (p) planes in Ti/Zr.

n	m	$A_{nm}^{Ti(b)}$	$B_{nm}^{Ti(b)}$	$A_{nm}^{Ti(p)}$	$A_{nm}^{Zr(b)}$	$B_{nm}^{Zr(b)}$	$A_{nm}^{Zr(p)}$
0	0	379.00		554.55	301.09		557.71
0	1			−351.05			−336.93
0	2	−109.35	−40.77	−56.29	−101.53	−74.90	−52.40
0	3			7.17			21.15
0	4	−5.68	9.71		3.15		
1	0			103.41			135.19
1	1	−210.34	76.20	−79.79	−195.16	142.55	−70.80
1	2			−105.76			−155.75
1	3	−34.35		−23.36	−13.12		−23.28
1	4						−12.62
1	5	4.40	−9.07			−6.26	−7.00
2	0	−15.68		−25.30	−5.02		−45.12
2	2	−10.37	−20.94		3.03		
2	3			−9.31			
2	4		8.77			6.27	
3	1	4.08	8.38		3.83	5.43	
3	3	−4.44	4.95			3.87	

(39). Note that the spatiotemporal evolutions of the edge and screw dislocation densities are coupled through the same misfit energy γ. The set of equations (40,41), featuring in particular the involvement of the derivatives $\partial\gamma/\partial\eta_{12}$ and $\partial\gamma/\partial\eta_{32}$ in addition to shear stresses in the driving forces for dislocation motion, is similar to existing models (e.g. (Wei,2009)). Our model was tested and validated by modeling dissociated edge and screw dislocations in $< 111 >$ planes in Al. In this validation process, we used the expression of the generalized stacking fault energy provided in reference (Schoeck,2012). The structure of a dissociated edge dislocation is shown in Fig.(6). The results are in very close agreement with Schoeck's results. For the basal and prismatic dislocations simulated in the present paper, the initial Burgers vector is $\mathbf{a} =< 11-20 >$. Its magnitude in basal planes is $0.29338nm$ for Ti and $0.32293nm$ for Zr, $0.29472nm$ for Ti and $0.32323nm$ for Zr in type-I prismatic planes. The shear modulus is taken as $\mu = 40GPa$ for Ti and $\mu = 36GPa$ for Zr. The Poisson modulus is $\nu = 0.34$ for Ti and $\nu = 0.38$ for Zr. The values of B^{α}, $\dot{\gamma}^{p*}$, T^{*} defined above for Al are used for Zr and Ti.

5.3. Edge and screw dislocation structures

Fig.(7) shows the relaxed configurations of initially compact basal edge and screw dislocations in Ti. Both edge and screw dislocations dissociate into partial mixed dislocations. The edge dislocation is more dissociated than the screw dislocation because it has higher internal shear stress field. The predicted dissociation paths on the generalized stacking fault energy landscape

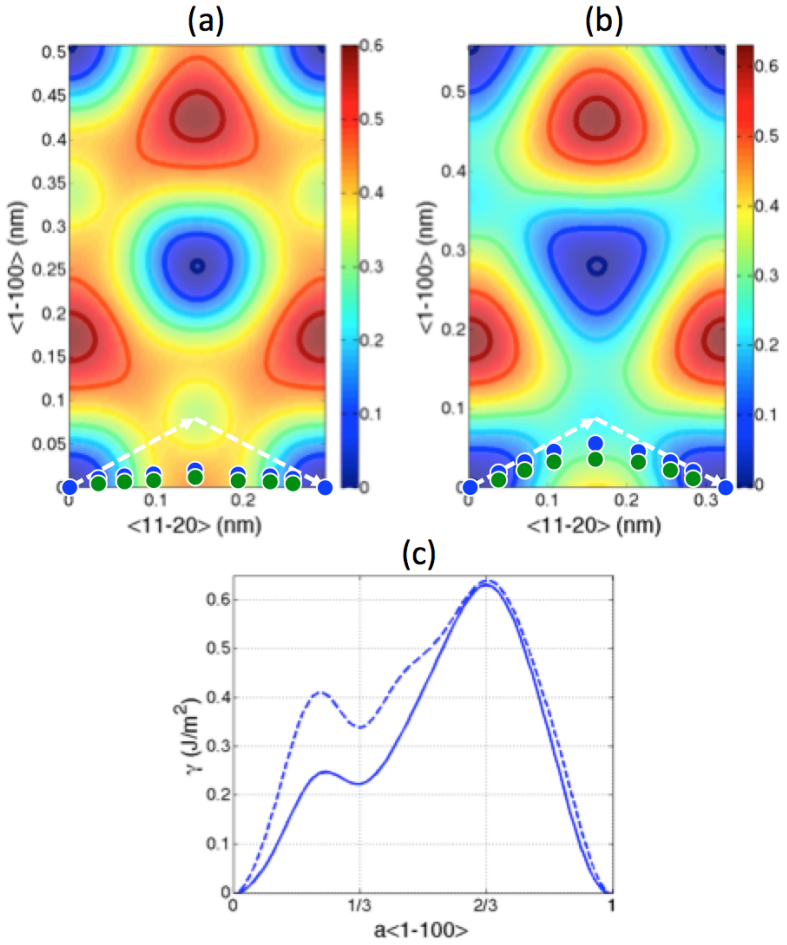

Figure 4: Generalized stacking fault energies in basal planes for (a) Ti and (b) Zr, as obtained from Ab-Initio calculations and approximated by Fourier series. The white-dotted arrows show the minimum generalized stacking fault energy paths for dissociation of the Burgers vector into partials. The blue/green spots show the paths corresponding to the relaxed dissociated edge/screw dislocation cores predicted by the model and shown in Figs.(7,8). In (c) are shown the energy profiles along $< 1-100 >$ type dissociation paths in Ti (dotted line) and Zr (solid line), the lattice parameter is a.

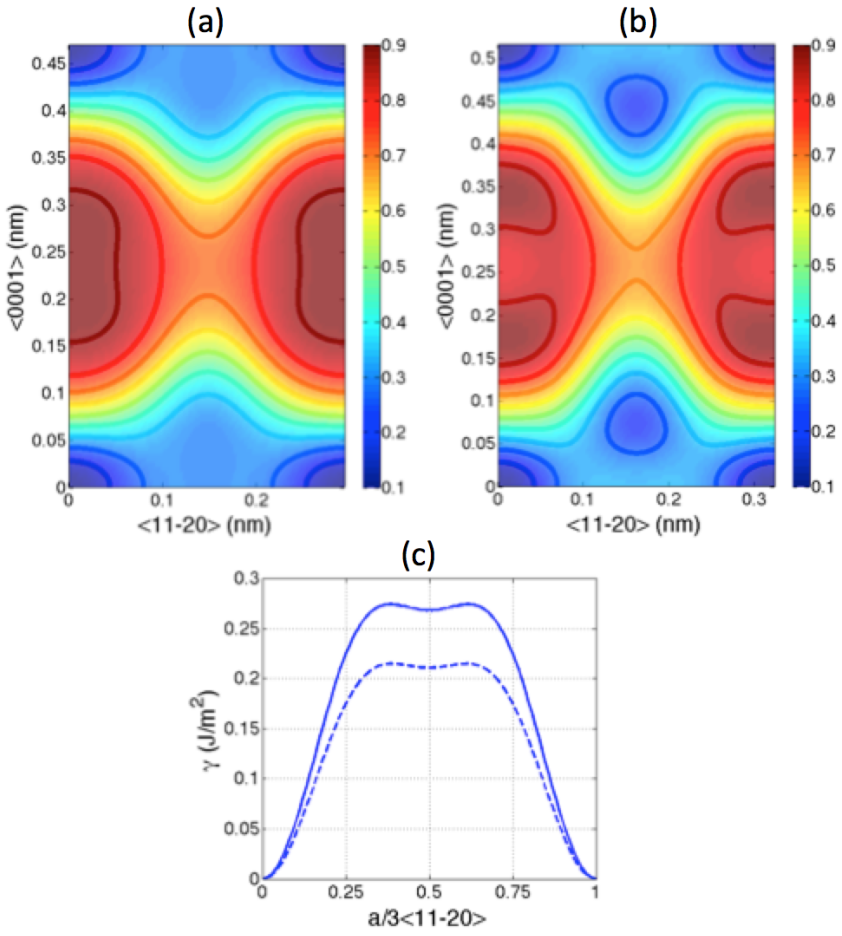

Figure 5: Generalized stacking fault energies in type-I prismatic planes for (a) Ti and (b) Zr, as obtained from Molecular Dynamics calculations and approximated by Fourier series. In (c) are shown the energy profiles along $< 11-20 >$ paths in Ti (dotted line) and Zr (solid line), the lattice parameter is a.

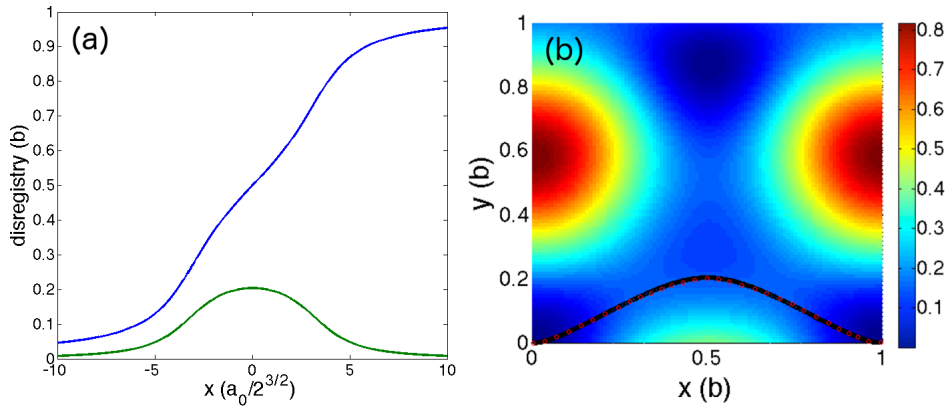

Figure 6: (a) spatial distribution of the predicted misfit components (blue: edge component, green: screw component) for a dissociated edge dislocation in Al, by using the gamma-surface from ref. (Schoeck,2012). (b) gamma-surface landscape (J/m^2) in Al by using the expression given in ref. (Schoeck,2012), and comparison of the predicted dissociation path for an edge dislocation with our model (black line) and that obtained in ref. (Schoeck,2012) (red circles). In both figures, x denotes the direction of the Burgers vector and a_0 the lattice parameter.

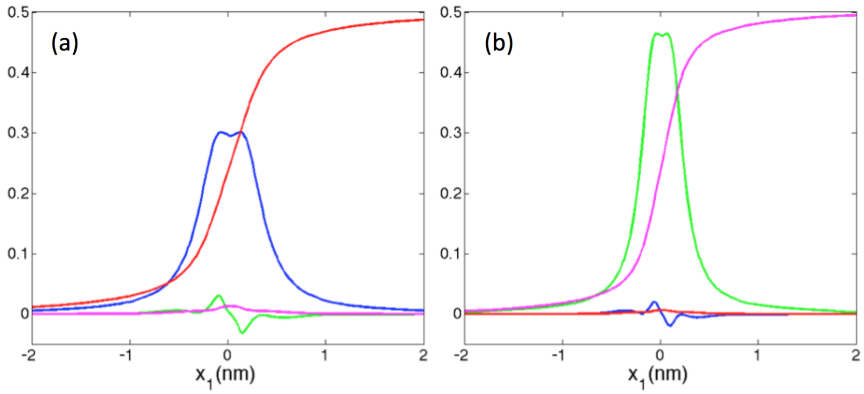

Figure 7: Relaxed dissociated structures of basal edge (a) and screw (b) dislocations in Ti. The blue curve is the edge dislocation density α^S_{13}, the red curve is the associated misfit η_{12} (in units of $2b$). The green curve is the screw dislocation density α^S_{33}, the magenta curve is the associated misfit η_{32} (in units of $2b$).

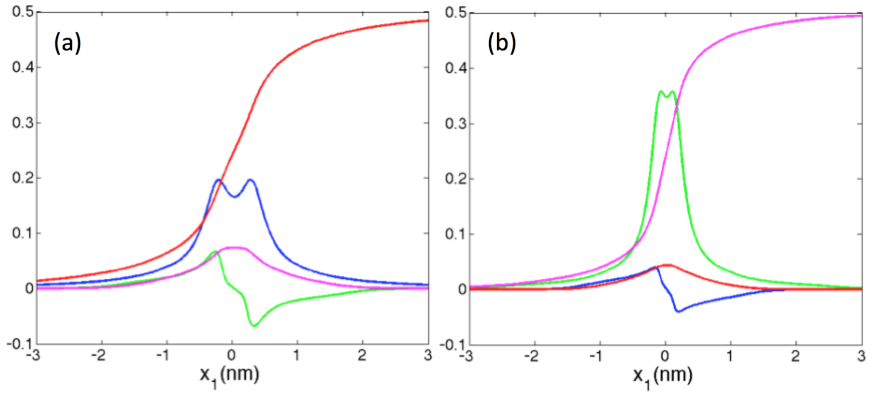

Figure 8: Relaxed dissociated structures of basal edge (a) and screw (b) dislocations in Zr. The blue curve is the edge dislocation density α^S_{13}, the red curve is the associated misfit η_{12} (in units of $2b$). The green curve is the screw dislocation density α^S_{33}, the magenta curve is the associated misfit η_{32} (in units of $2b$).

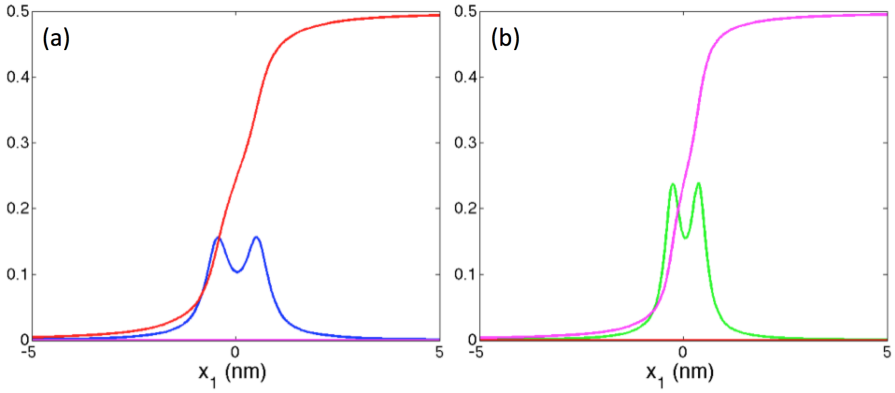

Figure 9: Relaxed dissociated structures of prismatic edge (a) and screw (b) dislocations in Ti. The blue curve is the edge dislocation density α^S_{13}, the red curve is the associated misfit η_{12} (in units of $2b$). The green curve is the screw dislocation density α^S_{33}, the magenta curve is the associated misfit η_{32} (in units of $2b$).

are displayed in Fig.(4.a). Interestingly, they do not superimpose with the minimal-energy ones. This property is not retrieved in the dissociation paths of dislocations in $< 111 >$ planes in Al (see Fig.(6.b)), which fall much closer to the minimum stacking fault energy paths (Denoual,2004; Hartford,1998). Such a result stems from (i) the difference in shape between the generalized stacking fault energy landscapes in Al and Ti, and (ii) the strong sensitivity of the dislocation core profiles to these energy landcapes. In particular, the ratio of the maximum value of the generalized stacking fault energy along the Burgers vector path to the intrinsic stacking fault energy, as well as the slope of the energy landscape in between these two values, play a key role in the dissociation process. The larger the ratio and the slope, the larger the driving force for dissociation. The ratio and slope are larger in Al than in the Ti basal plane simulated here. Fig.(8) shows the relaxed configurations of initially compact basal edge and screw dislocations in Zr. As compared to Ti and for the reasons just mentioned above, dislocation dissociation is more pronounced because the generalized stacking fault energy landscape is more favorable to dissociation (see Fig.(4)). However, the dissociated paths on the generalized stacking fault energy landscape displayed in Fig.(4.b) still do not superimpose with the minimum energy paths. Fig.(9) and Fig.(10) show the relaxed structures of edge and screw dislocations in prismatic planes in Ti and Zr, respectively. Here, dissociated dislocations are obtained, but the partial dislocations have the same Burgers vector directions that the full dislocations. This is clearly due to the shape of the

prismatic generalized stacking fault energy landscape (Fig.(5)). Further, a good agreement between our predicted Zr prismatic screw dislocation and that obtained in reference (Clouet,2012). We note that the overall Burgers vector of all simulated dislocations, as measured by integrating Eqs.(29,31) over the dislocation cores, is conserved during self-relaxation and dissociation processes. However, at the lower and local scale where differential dislocation elements building the dislocation cores are defined, the local partial Burgers vector direction may change, due to the dislocation source term introduced in the dislocation transport equation. The dissociation of edge and screw dislocations into mixed partials in basal planes cannot be predicted without this source term. Dislocation nucleation was also recently investigated in the field dislocation mechanics model, but rather by performing a stability analysis of the dislocation density transport equation in a finite strain setting (Garg,2015).

6. Motion and nucleation of dislocations

6.1. Motion and deformation of dislocation cores under applied stresses

We now investigate the motion of dislocation cores under an applied external shear stress. We first consider the dissociated relaxed structure of the Zr basal edge dislocation core shown in Fig.(8) as an initial condition, to which a uniform external shear stress T_{12}^{A} is imposed until the dislocation has moved sufficiently. Then, the shear stress is removed and the dislocation core is left self-relaxing from this possibly deformed configuration. Two

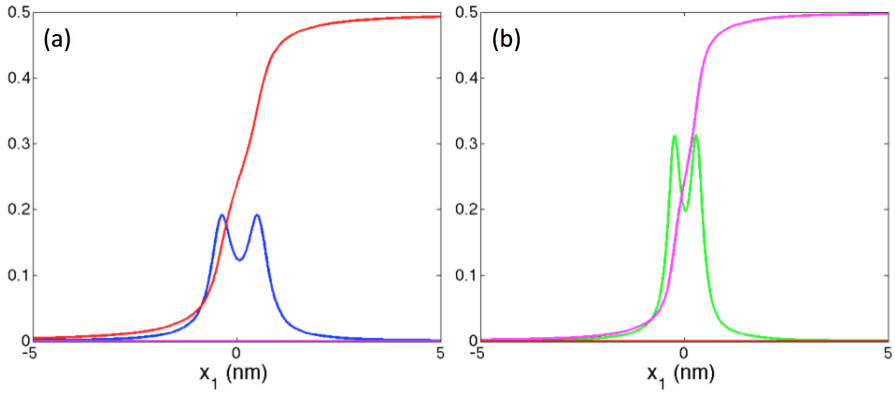

Figure 10: Relaxed dissociated structures of prismatic edge (a) and screw (b) dislocations in Zr. The blue curve is the edge dislocation density α^S_{13}, the red curve is the associated misfit η_{12} (in units of $2b$). The green curve is the screw dislocation density α^S_{33}, the magenta curve is the associated misfit η_{32} (in units of $2b$).

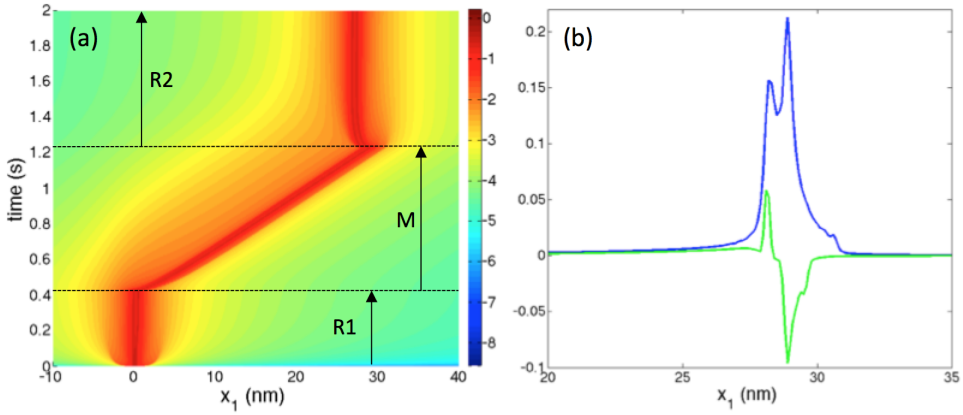

Figure 11: (a) Space-time diagram showing the motion of the dissociated basal edge dislocation in Zr shown in Fig.(8) under an applied shear stress of $T^A_{12} = 1GPa$ followed by self-relaxation after removal of the applied stress. Color-coded is shown the norm of the dislocation density tensor $(\alpha^S_{13}\alpha^S_{13} + \alpha^S_{33}\alpha^S_{33})^{1/2}$ (log10 scale). The diagram shows first the self-relaxation and dissociation of an initially compact edge dislocation core (R1), its subsequent motion and deformation under the applied shear stress, where the transient deformation of the core can be observed (M), and the self-relaxation of the dislocation core after removal of the applied stress, showing backsliding of the dislocation (R2). (b) Profile of the deformed dislocation core at the end of the loading sequence. The blue curve is the edge dislocation density α^S_{13} and the green curve is the screw dislocation density α^S_{33}.

values of the applied stress $T_{12}^A = 10MPa$ and $T_{12}^A = 1GPa$ are tested. For the low applied stress (10MPa), the dislocation core moves almost uniformly without deforming and no core self-relaxation is observed after the load is removed. For the high stress ($1GPa$), the core undergoes deformation as we detail below and as can be seen Fig.(11). The simulation presented in the latter figure is as follows. After initial self-relaxation and dissociation of the edge dislocation where the dislocation core reaches its low energy equilibrium configuration (time interval R1 in the figure), a stress of $1GPa$ is applied to set the dislocation into motion (M). During an initial transient regime, the leading partial moves faster than the trailing partial and its core encounters compression. The trailing partial spreads out, such that a tail forms behind the dislocation. As can be seen from the space-time slope in Fig.(11), the overall velocity of the dislocation significantly decreases during this deformation process, which acts as a rate-limiting factor. After this transient, a stable deformed dissociated dislocation core is obtained, which moves almost uniformly. The deformed core distribution is shown in Fig.(11.b) at the end of the loading sequence (M). The partial dissociation of the dislocation is reduced as compared to that of the relaxed configuration before loading. Interestingly, the deformed dislocation core is not an equilibrium configuration, and self-rearrangement occurs when the applied shear stress is removed (R2). The tail pulls back the rest of the dislocation and the leading partial spreads out, until the core retrieves the initial dissociated structure shown in Fig.(8). The full dislocation core moves back a few nanometers during this

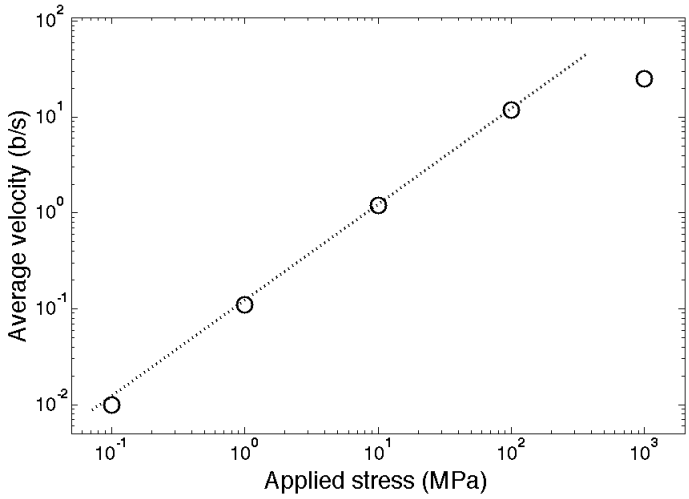

Figure 12: Log-Log plot of the average dislocation velocity as a function of applied shear stress during loading of an edge dislocation core obtained using the Peierls sinusoidal potential. The dotted line shows the linear slope.

anelastic relaxation process, which cancels part of the plastic slip produced during forward loading. Such a mechanism was also recently observed in the dislocation layer model (Zhang,2015). If the dislocation core is not allowed to self-relax and a reverse shear stress of same amplitude is applied immediately after forward shear loading, then a 35% instantaneous increase of the plastic strain rate is observed at stress reversal, indicating the existence of a back-stress effect at the scale of the dislocation core. Such a phenomenon was observed at a macroscopic scale, at stress reversal during the forward-reverse torsion of ice single crystals (Taupin,2007).

To further investigate the relationship between the applied stress, the core

deformation and the dislocation velocity, we plot in Fig.(12) an averaged measure of the velocity of the edge dislocation core vs. the applied shear stress, as obtained from the Peierls sinusoidal misfit energy. The velocity is measured as the ratio of the difference of position of the dislocation density peak value, over the time needed for that motion. The dislocation is left to move over a sufficiently large distance such that an average measure is reasonable. When the applied stress lies in the range $0.1MPa - 100MPa$, the dislocation core moves without significantly deforming. In this range, the averaged velocity vs. stress curve follows a linear trend as can be seen in Fig.(12). Such behaviour can be expected from the linear viscous drag relationship used in the model. However, as already indicated for the dissociated basal edge dislocation shown in Fig.(11), significant deformation of the core takes place and the averaged dislocation velocity is significantly reduced when the applied stress reaches $1GPa$. The averaged velocity is found to be lower by a factor 4 than the value expected from the linear trend. Hence, the linear relationship between the differential dislocation velocity and the applied stress is not reflected in the averaged dislocation velocity at high stresses, which behaves non-linearly. To further check this result, a space-averaged velocity of the dislocation profile was also taken and the loading time and distance travelled by the dislocation were made sufficiently large to allow calculating an average in time of this space-averaged velocity. The reduction of dislocation velocity, as well as the low stress linear behaviour, are retrieved by using this refined measure method. We note that the order

of magnitude for the dislocation velocity reported in Fig.(12) is much lower than that of shear wave speeds. In our simulations, the dislocation velocity and the associated time scale directly derive from the value of the drag coefficient used in the dislocation velocity. Clearly, our results suggest that the value of the drag coefficient we used is much too high, leading to very low dislocation velocities and very large travelling times. For the applied stress of $0.01MPa$, no average dislocation motion is clearly observed, but the numerical fluctuations on the velocity of the differential dislocation elements are such that no firm conclusion can presently be reached. Note however that (Zhang,2015) predicted a critical stress for dislocation glide by using a dislocation layer model similar to ours.

6.2. Nucleation of dislocation loops

In a recent study (Miller,2008; Acharya,2008), it was shown by analysing atomistic simulations of dislocation dipole nucleation during nano-indentation that the main difference between dislocation nucleation and dislocation motion is the much larger number of atoms that need to be moved in nucleating a dislocation dipole (or loop in a 3D setting). Otherwise, like dislocation motion, the nucleation mechanism is a dissipative process in which elastic strains are relaxed by the production of plastic slip. Thus, it was shown that the Field Dislocation Mechanics framework might be adequately used to model dislocation nucleation and subsequent motion. For this, the dislocation transport equation that renders the motion of dislocation densities

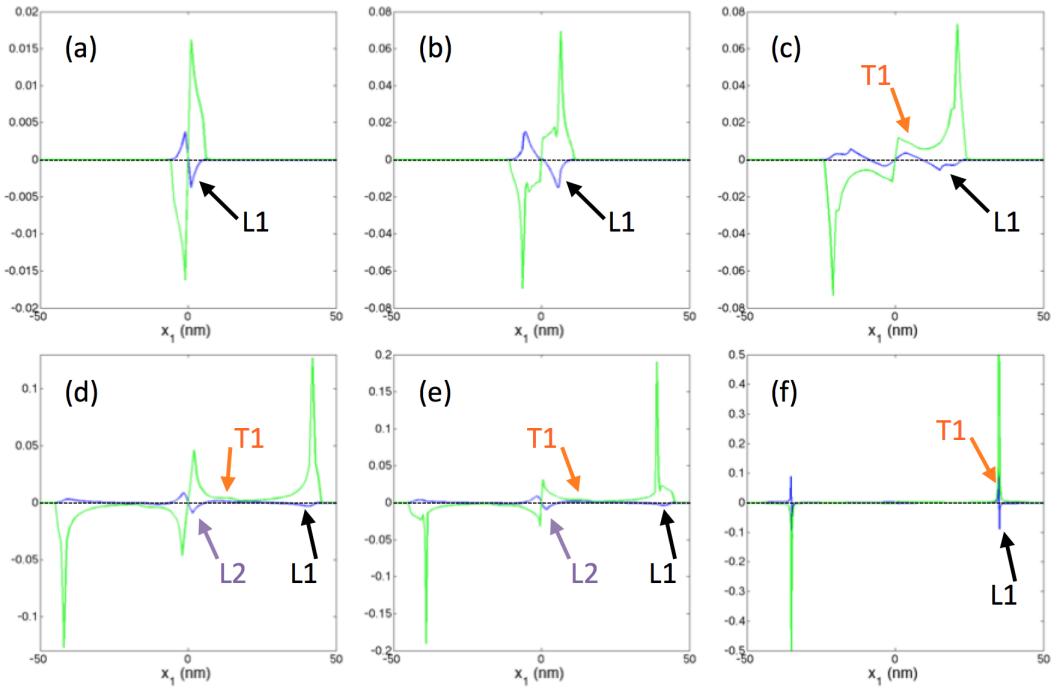

Figure 13: Nucleation and expansion of a dissociated screw dislocation dipole in basal plane in Zr under a localised shear stress in the middle of the glide plane. A homogeneous shear stress $T_{12}^A = 5GPa$ is applied in the glide plane, except in a narrow central region where it is $6GPa$. The edge dislocation density α_{13}^S is shown in blue solid line and the screw dislocation density α_{33}^S is shown in green solid line. The right part of the dipole evolves as follows: Nucleation of a first leading partial L1 (a), propagation of the leading partial L1 (b), nucleation of the first trailing partial T1 (c), glide of the first partial L1 and viscous deformation of the first trailing partial T1, nucleation of a second leading partial L2 (d). Panel (e) shows the self-relaxation of the dislocations when the applied load is removed. The first leading partial L1 glides back, the first trailing partial T1 glides towards the leading partial L1 and the second leading partial L2 annihilates with that on its left. Panel (f) shows the relaxed dissociated screw dislocation dipole composed of partials L1 and T1. The second dipole has been annihilated.

has to be complemented by a nucleation potential term whose meaning is the production of plastic slip due to dislocation nucleation. The kinematics and thermodynamics framework that we used corresponds to that developed in reference (Acharya,2008). The aim of this Section is thus to check whether our model can predict the nucleation of a dislocation dipole, corresponding in our model to two opposite dislocations or dislocation partials. Considering again Zirconium, we start from a basal plane free of any dislocation density. A homogeneous shear stress $T_{32}^{A} = 5GPa$ is applied uniformly in this plane, except for a narrow central patch where it is $6GPa$. We expect the strong shear stress gradients at the edges of this central region to generate dislocation dipoles that will then expand in the glide plane. The simulation results are shown in Fig.(13). Through the incompatible plastic distortion rate $\dot{\mathbf{U}}^{p*}$ in Eq.(8) inducing the dislocation source term in Eq.(9), plastic strain is produced in the central region of the plane, which corresponds to the nucleation of a screw dislocation dipole. Nucleation starts by the formation of a dipole of leading partials in the strong stress gradient areas (Fig.13.a) and their gliding away in the basal plane (Fig.13.b). The nucleation and glide of trailing partials follow (Fig.(13.c,d)). A dissociated screw dislocation loop has thus been formed. Note the large distance between the leading and trailing partials as well as the significant viscous spread of the trailing partials, arise from the large stresses applied and the dislocation velocity viscous law that we used. After nucleation of the first loop, a second dislocation loop starts to form, and the whole process could be re-iterated. However, we remove

the applied shear stress once the leading partials of the second dislocation loop are nucleated. Self-relaxation of the dislocation cores is then observed (Fig.(13.e,f)). Interestingly, although the distance between the first leading and trailing partial dislocations is large at stress removal, they rearrange in such a way that the narrow dissociated dislocation core structure shown in Fig.(8) is retrieved. The leading partials of the second loop glide back and annihilate each other, such that only the first dislocation loop remains visible in the basal plane.

7. Conclusion

The elasto-plastic theory of dislocation fields has been used to model the structure of planar dislocation cores in crystalline materials. In the context of isotropic linear elasticity, the theory is such that endless relaxation of dislocation cores occurs if no counter - balancing force is introduced to oppose the internal shear stress. Based on the Peierls-Nabarro model and its recent extensions, a non-convex periodic misfit surface energy is added to the convex isotropic elastic potential. Through the derivation of thermodynamically consistent driving forces, this additional energy allows defining restoring stresses that lead to compact equilibrium core configurations. The model retrieves the Peierls-Nabarro elasto-static solution for a sinusoidal potential. Interestingly, the relaxation of two arbitrary dislocation distributions by dissipative dislocation transport converges toward the Peierls-Nabarro solution, suggesting that this core profile can be reached through dynamic processes.

When introducing generalized stacking fault energies in the model, dissociation of dislocation cores into partials can be predicted. The model was in particular applied to the self-relaxation and dissociation of edge and screw dislocations in basal and prismatic planes in titanium and zirconium. It was shown that dissociation occurs in basal and prismatic planes, and that for basal dislocations, the dissociation paths on the generalized stacking fault energy landscape do not correspond to the minimum energy path. Motion and deformation of dislocation cores under applied shear stress can also be predicted. Remarkably, the model predicts viscosity effects on dislocation core shape and velocity, as well as anelastic relaxation at dislocation core level when shear loading is interrupted, and kinematic hardening features when it is reversed. Hence, the present simple one-dimensional model provides a rather fine description of dislocation planar structures and their deformation and motion under stress. Further, it helps understanding fundamental questions pertaining to the equilibrium and stability of defect cores within a dynamic dislocation field continuum mechanics framework.

Appendix A: DFT calculations of generalized stacking fault energies

The ab-initio calculations were performed on the basis of the Density Functional Theory (DFT) (Kohn,1965; Hohenberg,1964), using Vienna ab initio software package (Hafner,2000; Kresse,1996a; Kresse,1996b; Vasp,2015). The

interaction between ions and electrons is described by ultra-soft pseudopotentials (USPP) (Vanderbilt,1990). The generalized gradient approximation (GGA) in Perdew and Wang parametrization (Kresse,1996c; Perdew,1991) is used to describe the exchange-correlation energy. For the pseudopotentials we used, the electronic configurations are (3d34s1) for Ti and (4d35s1) for Zr, and the kinetic energy cutoff is 300eV. For the unit cell, tests were carried out using different k-point meshes to ensure absolute convergence of the total energy with an accuracy better than 10^{-3} eV/atom. The optimal choice for the Monkhorst-Pack grid (Monkhorst,1976) is a 8 k-point grid within a unit cell. The density of k-points in the unit cell is kept in the supercells and the kinetic energy cutoff is unchanged. All the structures have been relaxed using the conjugate gradient algorithm and both the atomic position and volume have been optimized (Poty,2011). We have used the unit cell to calculate the structural properties (lattice parameters and cohesive energy). The interface energies are obtained using supercells. The latter are multiples of the unit cell composed of two motifs. A convergence study of the distance between the sheared interface and its periodic image was carried out. It showed that for a distance larger than 1.5nm, the variations of the interface energy become negligible. For the maps of interface energy, we used a sampling of 25×40 points for the basal and type-I prismatic planes, for both zirconium and titanium gliding systems.

Appendix B: Molecular Statics calculations of generalized stacking

fault energies

A laboratory-made code is used. The volume, temperature and number of atoms are fixed (NVT ensemble). The simulations are performed at $0K$. The Newtonian equations of motion are integrated using a fifth-order Gear predictor-corrector algorithm. Lagrange polynomials are used to fit the tabulated interatomic potential table. For each calculation, the relaxed structures are obtained by minimizing the energy. The convergence of the energy was reached and the error in the energy was found to be less than $0.0001eV$. The potentials we used in this work rely on the Embedded Atom Method (EAM) (Daw,1993; Daw,1984; Baskes,1994). The stacking fault energy maps are calculated with a box containing 8000 atoms. The box is divided into two smaller boxes. The first box is fixed while the second one is shifted in two directions. The relaxation of each atom is possible only in the third direction by MS quenching.

Appendix C: Useful mathematical notations

A bold symbol denotes a tensor. When there may be ambiguity, an arrow is superposed to represent a vector: $\vec{\mathbf{V}}$. The symmetric part of tensor $\mathbf{A}$ is denoted $\mathbf{A}^{sym}$. Its skew-symmetric part is $\mathbf{A}^{skew}$. The tensor $\mathbf{A}.\mathbf{B}$, with rectangular Cartesian components $A_{ik}B_{kj}$, results from the dot product of tensors $\mathbf{A}$ and $\mathbf{B}$, and $\mathbf{A} \otimes \mathbf{B}$ is their tensorial product, with components

$A_{ij}B_{kl}$. A : represents the trace inner product of the two second order tensors $\mathbf{A} : \mathbf{B} = A_{ij}B_{ij}$, in rectangular Cartesian components, or the product of a higher order tensor with a second order tensor, e.g., $\mathbf{A} : \mathbf{B} = A_{ijkl}B_{kl}$. The cross product $\mathbf{A} \times \mathbf{V}$ of a second-order tensor $\mathbf{A}$ and a vector $\mathbf{V}$, the **div** and **curl** operations for second-order tensors are defined row by row, in analogy with the vectorial case. For any base vector $\mathbf{e}_i$ of the reference frame:

$$(\mathbf{A} \times \mathbf{V})^t.\mathbf{e}_i = (\mathbf{A}^t.\mathbf{e}_i) \times \mathbf{V} \tag{44}$$

$$(\mathbf{div}\ \mathbf{A})^t.\mathbf{e}_i = \mathbf{div}(\mathbf{A}^t.\mathbf{e}_i) \tag{45}$$

$$(\mathbf{curl}\ \mathbf{A})^t.\mathbf{e}_i = \mathbf{curl}(\mathbf{A}^t.\mathbf{e}_i). \tag{46}$$

In rectangular Cartesian components:

$$(\mathbf{A} \times \mathbf{V})_{ij} = e_{jkl}A_{ik}V_l \tag{47}$$

$$(\mathbf{divA})_i = A_{ij,j} \tag{48}$$

$$(\mathbf{curlA})_{ij} = e_{jkl}A_{il,k}. \tag{49}$$

where e_{jkl} is a component of the third-order alternating Levi-Civita tensor $\mathbf{X}$. A vector $\vec{\mathbf{A}}$ is associated with tensor $\mathbf{A}$ by using its trace inner product with tensor $\mathbf{X}$:

$$(\vec{\mathbf{A}})_k = -\frac{1}{2}(\mathbf{A} : \mathbf{X})_k = -\frac{1}{2}e_{ijk}A_{ij}. \tag{50}$$

In the component representation, the spatial derivative with respect to a Cartesian coordinate is indicated by a comma followed by the component index. A superposed dot represents a material time derivative.

References

[Acharya,2001] Acharya, A., 2001. A model of crystal plasticity based on the theory of continuously distributed dislocations, J. Mech. Phys. Solids **49**, 761.

[Acharya,2003] Acharya, A., 2003. Driving forces and boundary conditions in continuum dislocation mechanics, Proc. Royal Society **A 459**, 1343.

[Acharya,2008] Acharya, A., Beaudoin, A.J., Miller, R.E., 2008. New perspectives in plasticity theory: Dislocation nucleation, waves, and partial continuity of plastic strain rate, Mathematics and Mechanics of Solids **13**, 292.

[Baskes,1994] Baskes, M.I., Johnson, R.A., 1994. Modified embedded atom potentials for HCP metals, Model Simul Mater Sci Eng **2**, 147.

[Berbenni,2014] Berbenni, S., Taupin, V., Djaka, K.S., Fressengeas, C., 2014. A numerical spectral approach for solving elasto-static field dislocation and g-disclination mechanics, Int. J. Solids Structures **51**, 4157.

[Chu,2013] Chu, H.J., Wang, J., Beyerlein, I.J., Pan, E., 2013. Dislocation models of interfacial shearing induced by an approaching lattice glide dislocation, Int. J. Plasticity **41**, 1.

[Clouet,2012] Clouet, E., 2012. Screw dislocation in zirconium: An ab initio study, Phys. Rev. B **86**, 144104.

[Daw,1993] Daw, S., Foiles, S.M., Baskes, M.I., 1993. EAM: a review of theory and application, Mater. Sci. Rep. **9**, 251.

[Daw,1984] Daw, M.S., Baskes, M.I., 1984. Embedded-atom method: Derivation and application to impurities, surfaces, and other defects in metals, Phys. Rev. B **29**, 6443.

[Denoual,2004] C. Denoual, 2004. Dynamic dislocation modeling by combining Peierls Nabarro and Galerkin methods, Physical Review B **70**, 024106.

[Denoual,2007] C. Denoual, 2007. Modeling dislocation by coupling Peierls-Nabarro and element-free Galerkin methods, Comput. Methods Appl. Mech. Eng. **196**, 1915.

[Djaka,2015] Djaka, K.S., Taupin, V., Berbenni, S., Fressengeas, C., 2015. A numerical spectral approach to solve the dislocation density transport equation, Modelling Simul. Mater. Sci. Eng. **23**, 065008.

[Fressengeas,2011] Fressengeas, C., Taupin, V., Capolungo, L., 2011. An

elasto-plastic theory of dislocation and disclination fields, Int. J. Solids Structures **48**, 3499.

[Fressengeas,2011b] Fressengeas, C., Acharya, A., Beaudoin, A.J., 2011. Dislocation mediated continuum plasticity: case studies on modeling scale-dependence, scale-invariance, and directionality of sharp yield point, in Computational Methods for Microstructure-Property Relationships, Springer, edited by S. Ghosh and D. Dimiduk, 277-309.

[Garg,2015] Garg, A., Acharya, A., Maloney, C.E., 2015. A study of conditions for dislocation nucleation in coarser-than-atomistic scale models, J. Mech. Phys. Solids **75**, 76.

[Hafner,2000] Hafner, J., 2000. Atomic-scale computational materials science, Acta Mater. **48**, 71.

[Hartford,1998] Hartford, J., von Sydow, B., Wahnström, G., Lundqvist, B.I., 1998. Peierls barriers and stresses for edge dislocations in Pd and Al calculated from first principles, Phys. Rev. B **58**, 2488.

[Hohenberg,1964] Hohenberg, P., Kohn, W., 1964. Inhomogeneous Electron Gas, Phys. Rev. **136**, B864.

[Hu,2004] Hu, S.Y., Li, Y.L., Zheng, Y.X., Chen, L.Q., 2004. Effect of solutes on dislocation motion - a phase-field simulation, Int. J. Plasticity **20**, 403.

[Hunter,2014] Hunter, A., Beyerlein, I.J., 2014. Stacking fault emission from grain boundaries: Material dependencies and grain size effects, Mater. Sci. Eng. A **600**, 200.

[Joós,1994] Joós, B., Ren, Q., Duesbery, M.S., 1994. Peierls-Nabarro model of dislocations in silicon with generalized stacking-fault restoring forces, Phys. Rev. B **50**, 5890.

[Kresse,1996a] Kresse, G., Furthmüller, J., 1996. Efficient iterative schemes for ab initio total-energy calculations using a plane-wave basis set, Phys. Rev. B **54**, 11169.

[Kresse,1996b] Kresse, G., Furthmüller, J., 1996. Efficiency of ab-initio total energy calculations for metals and semiconductors using a plane-wave basis set, Comput. Mater. Sci. **6**, 15.

[Kresse,1996c] Kresse, G., Hafner, J., 1996. Norm-conserving and ultrasoft pseudopotentials for first-row and transition elements, J. Phys.: Condens. Matter **6**, 8245.

[Kohn,1965] Kohn, W., Sham, L.J., 1965. Self-Consistent Equations Including Exchange and Correlation Effects, Phys. Rev. **140**, A1133.

[Kröner,1980] Kröner, E., 1980. Continuum model of defects, in Physics of Defects, Ed. R. Balian et al., North Holland, Amsterdam, 218.

[Lu,2000] Lu, G., Kioussis, N., Bulatov, V.V., Kaxiras, E., 2000.

Generalized-stacking-fault energy surface and dislocation properties of aluminum, Phys. Rev. B **62**, 3099.

[Lu,2004] Lu, G., Bulatov, V.V., Kioussis, N., 2004. On stress assisted dislocation constriction and cross-slip, Int. J. Plasticity **20**, 447.

[Metsue,2010] Metsue, A., Carrez, P., Denoual, C., Mainprice, D., Cordier, P., 2010. Peierls-Nabarro modelling of dislocations in diopside, Phys. Chem. Minerals **37**, 711.

[Miller,2008] Miller, R.E., Rodney, D., 2008. On the nonlocal nature of dislocation nucleation during nanoindentation, J. Mech. Phys. Solids **56**, 1203.

[Monkhorst,1976] Monkhorst, H.J., Pack, J.D., 1976. Special points for Brillouin-zone integrations, Phys. Rev. B **13**, 5188.

[Mura,1963] Mura, T., 1963. Continuous distributions of moving dislocations, Phil. Mag. **89**, 843.

[Nabarro,1947] Nabarro, F.R.N., 1947. Dislocations in a simple cubic lattice, Proc. Phys. Soc. **59**, 256.

[Nye,1953] Nye, J.F., 1953. Some geometrical relations in dislocated crystals, Acta Metall. **1**, 153.

[Peierls,1940] Peierls, R., 1940. The size of a dislocation, Proc. Phys. Soc. **52**, 34.

[Perdew,1991] Perdew, J.P., Wang, Y., 1991. Accurate and simple analytic representation of the electron-gas correlation energy, Phys. Rev. B **45**, 13244.

[Pi,2016] Pi, Z.P., Fang, Q.H., Liu, B., Feng, H., Liu, Y., Liu, Y.W., Wen, P.H., 2016. A phase field study focuses on the transverse propagation of deformation twinning for hexagonal-closed packed crystals, Int. J. Plasticity **76**, 130.

[Poty,2011] Poty, A., Raulot, J.M., Xu, H., Bai, J., Schuman, C., Lecomte, J.S., Philippe, M.J., Esling, C., 2011. Classification of the critical resolved shear stress in the hexagonal-close-packed materials by atomic simulation: Application to α-zirconium and α-titanium, J. Appl. Phys. **110**, 014905.

[Roy,2005] Roy, A., Acharya, A., 2005. Finite element approximation of field dislocation mechanics, J. Mech. Phys. Solids **53**, 143.

[Schoeck,2012] Schoeck, G., 2012. The core structure and Peierls potential of dislocations in Al, Mater. Sci. Eng. A **558**, 162.

[Shen,2004] Shen, C., Wang, Y., 2004. Incorporation of γ-surface to phase field model of dislocations: simulating dislocation dissociation in fcc crystals, Acta Mater. **52**, 683.

[Sun,2016] Sun, X.-Y., Taupin, V., Fressengeas, C., Cordier, P., 2016. Continuous description of the atomic structure of grain boundaries using

dislocation and generalized-disclination density fields, Int. J. Plasticity **77**, 75.

[Taupin,2007] Taupin, V., Varadhan, S., Chevy, J., Fressengeas, C., Beaudoin, A.J., Montagnat, M., Duval, P., 2007. Effects of Size on the Dynamics of Dislocations in Ice Single Crystals, Phys. Rev. Lett. **99**, 155507.

[Taupin,2014] Taupin, V., Capolungo, L., Fressengeas, C., 2014. Disclination mediated plasticity in shear-coupled boundary migration, Int. J. Plasticity **53**, 179.

[Tucker,2015] Tucker, G.J., Foiles, S.M., 2015. Quantifying the influence of twin boundaries on the deformation of nanocrystalline copper using atomistic simulations, Int. J. Plasticity **65**, 191.

[Vanderbilt,1990] Vanderbilt, D., 1990. Soft self-consistent pseudopotentials in a generalized eigenvalue formalism, Phys. Rev. B **41**, 7892.

[Varadhan,2006] Varadhan, S., Beaudoin, A.J., Acharya, A., Fressengeas, C. 2006. Dislocation transport using an explicit Galerkin-Least Squares formulation, Modelling Simul. Mater. Sci. Eng. **14**, 1245.

[Vasp,2015] http://www.vasp.at

[Wang,2008] Wang, J., Hoagland, R.G., Hirth, J.P., Misra, A., 2008. Atomistic modeling of the interaction of glide dislocations with weak interfaces, Acta Mater. **56**, 5685.

[Wang,2014] Wang, J., Sehitoglu, H., Maier, H.J., 2014. Dislocation slip stress prediction in shape memory alloys, Int. J. Plasticity **54**, 247.

[Wei,2009] Wei, H., Xiang, Y., 2009. A generalized Peierls-Nabarro model for kinked dislocations, Phil. Mag. **89**, 2333.

[Zeng,2016] Zeng, Y., Hunter, A., Beyerlein, I.J., Koslowski, M., 2016. A phase field dislocation dynamics model for a bicrystal interface system: An investigation into dislocation slip transmission across cube-on-cube interfaces, Int. J. Plasticity, **79**, 293.

[Zhang,2015] Zhang, X., Acharya, A., Walkington, N.J., Bielak, J., 2015. A single theory for some quasi-static, supersonic, atomic, and tectonic scale applications of dislocations, J. Mech. Phys. Solids **84**, 145.

[Zhang,2016] Zhang, Y., Liu, J., Chu, H., Wang, J., 2016. Elastic fields of a core-spreading dislocation in anisotropic bimaterials, Int. J. Plasticity **81** ,231.